Correspondence to:
J. Saur,
jsaur@uni-koeln.de

Author Contributions:
Conceptualization: J. Saur
Data curation: J. Saur, D. Grodent
Formal analysis: A. Marzok, S. Schlegel
Funding acquisition: J. Saur
Investigation: J. Saur, D. Grodent, D. F. Strobel, K. D. Retherford
Methodology: A. Marzok, S. Schlegel, J. Saur
Project Administration: J. Saur
Software: A. Marzok, S. Schlegel, L. Roth
Supervision: J. Saur
Validation: S. Schlegel, J. Saur
Visualization: A. Marzok, S. Schlegel, L. Roth
Writing – original draft: A. Marzok, J. Saur

Mapping the Brightness of Ganymede's Ultraviolet Aurora Using Hubble Space Telescope Observations

A. Marzok[1], S. Schlegel[1] , J. Saur[1] , L. Roth[2] , D. Grodent[3] , D. F. Strobel[4] , and K. D. Retherford[5,6]

[1]Institute of Geophysics and Meteorology, University of Cologne, Cologne, Germany, [2]School of Electrical Engineering, KTH Royal Institute of Technology, Stockholm, Sweden, [3]Laboratoire de Physique Atmosphérique et Planétaire, STAR Institute, University of Liège, Liège, Belgium, [4]Department of Earth and Planetary Science, and Department of Physics and Astronomy, The Johns Hopkins University, Baltimore, MD, USA, [5]Southwest Research Institute, San Antonio, TX, USA, [6]University of Texas at San Antonio, San Antonio, TX, USA

Abstract We analyze Hubble Space Telescope observations of Ganymede made with the Space Telescope Imaging Spectrograph between 1998 and 2017 to generate a brightness map of Ganymede's oxygen emission at 1,356 Å. Our Mercator projected map demonstrates that the brightness along Ganymede's northern and southern auroral ovals strongly varies with longitude. To quantify this variation around Ganymede, we investigate the brightness averaged over 36°-wide longitude corridors centered around the sub-Jovian (0° W), leading (90° W), anti-Jovian (180° W), and trailing (270° W) central longitudes. In the northern hemisphere, the brightness of the auroral oval is 3.7 ± 0.4 times lower in the sub-Jovian and anti-Jovian corridors compared to the trailing and leading corridors. The southern oval is overall brighter than the northern oval, and only 2.5 ± 0.2 times fainter on the sub- and anti-Jovian corridors compared to the trailing and leading corridors. This demonstrates that Ganymede's auroral ovals are strongly structured in auroral crescents on the leading side (plasma downstream side) and on the trailing side (plasma upstream side). We also find that the brightness is not symmetric with respect to the 270° meridian, but shifted by ∼20° towards the Jovian-facing hemisphere. Our map will be useful for subsequent studies to understand the processes that generate the aurora in Ganymede's non-rotationally driven, sub-Alfvénic magnetosphere.

Plain Language Summary Northern lights often illuminate the night sky in a shimmering green or red tone at high geographic latitudes. This emission, scientifically referred to as *aurora*, is a result of electrically charged particles that move along Earth's magnetic field lines and interact with its atmosphere to produce auroral emission. Apart from the Earth, multiple other planets in our solar system also exhibit auroral emission. By characterizing the brightness and structure of these lights, we are therefore able to deduce insights about a planet's atmosphere, magnetic field and the physical processes occurring along the field lines from afar. In this work, we used observations from the Hubble Space Telescope to analyze the auroral emission of Jupiter's largest moon Ganymede. We combined multiple images of Ganymede to create the first complete map that displays the auroral brightness. Our map revealed that the emission on Ganymede's auroral ovals varies strongly in brightness with divisions into two distinct bright and faint regions. They resemble two auroral crescents in the north and south respectively, and demonstrate the uniqueness of Ganymede's aurora in comparison with the auroral ovals of other planets in the solar system.

1. Introduction

Being the only known moon in our solar system with an internal dynamo magnetic field (Kivelson et al., 1996, 2002), Jupiter's largest satellite Ganymede exhibits auroral emission structured by its magnetic field. The first hint of polar auroral emission at Ganymede was found by Hall et al. (1998) who used the Goddard High Resolution Spectrograph on the Hubble Space Telescope (HST) to observe Ganymede's trailing hemisphere in the FUV. The retrieved peaks in the spectrum around 1,304 and 1,356 Å were interpreted as emission from a tenuous oxygen atmosphere. The observed double-peak profile of the 1,356 Å emissions indicated that the emissions are spatially confined to the moon's magnetic north and south poles, suggesting auroral emissions (Hall et al., 1998). The species responsible for the emissions was determined from the detected flux ratios of OI 1,304 Å and OI 1,356 Å to be primarily molecular oxygen via dissociative electron-impact excitation. Feldman et al. (2000) first imaged the auroral emission with the Space Telescope Imaging Spectrograph (STIS) on the HST. The obtained

images of the upstream hemisphere depicted diffuse background emission with localized bright regions of 300 R at latitudes of approximately ±40°. Evaluating Galileo spacecraft data, Eviatar et al. (2001) argued that the measured population of thermal electrons $n_e \approx 5 - 20 \, \mathrm{cm}^{-3}$ with a temperature of 20 eV are not able to create even the diffuse background emission and that existing supra-thermal electrons of 2 keV are too few with a density of only $n_e \approx 0.5 - 2 \, \mathrm{cm}^{-3}$ to be responsible for the aurora as well. Therefore an additional process is required to accelerate the electrons to sufficient energies that could produce the emission.

From HST observations of the downstream and upstream hemispheres, McGrath et al. (2013) created a map of the location of Ganymede's auroral bands at 1,356 Å. Their results showed that the emission is correlated with Ganymede's plasma environment. The magnetospheric plasma of Jupiter is approximately corotating with its magnetic field at a synodic rotation period of 10.5 hr. As Ganymede is orbiting Jupiter in a synchronized rotation period of only 7.2 days, the bulk plasma flow therefore overtakes the moon on its orbit. On the orbitally trailing hemisphere, where the plasma streams towards the moon, the auroral bright spots are mapped to latitudes of 40°–55°. On the other hemisphere, that is, the downstream hemisphere, the brightest auroral emissions are found to be much closer to the equator near latitudes of only 10°–30° (McGrath et al., 2013; Musacchio et al., 2017). In this work we use the terminology "orbitally leading side" which corresponds to the "plasma downstream side" and "orbitally trailing side" which corresponds to the "plasma upstream side" interchangeably, depending on the physical context. These hemispheres are displayed in Figure 1 for visual orientation.

The aurora was further characterized by Musacchio et al. (2017), who also collectively analyzed STIS HST images from 1998, 2000, 2010, and 2011. Their findings include that the aurora changes position with the moon's changing location in Jupiter's magnetosphere. When Ganymede is inside the Jovian current sheet, the upstream emission is shifted by +2.9° towards higher latitudes and by −4.1° towards the equator on the downstream hemisphere. The authors also found that the total disk brightness is on average 1.4 times greater on the downstream side than on the upstream side. When Ganymede is located inside the current sheet compared to outside the current sheet, the brightness on the downstream side increases by a factor of 1.5 and decreases by 0.8 on the upstream side. By averaging the temporal effects of the various observed positions of the aurora, Musacchio et al. (2017) further characterized Ganymede's internal magnetic field and derived a modified position for the longitude of its dipole. The temporal effects were also studied by Saur et al. (2015), who used the oscillation of the aurora to demonstrate the presence of an ocean beneath Ganymede's icy crust from HST observations. The oscillation arises from Jupiter's time-varying magnetic field in the rest frame of Ganymede. Further details about the hydrogen corona and oxygen atmosphere of Ganymede were published recently in the works of Molyneux et al. (2018) and Alday et al. (2017). Alday et al. (2017) used data from 4 STIS campaigns between 1998 and 2014 to determine the abundance and variation of atomic hydrogen around Ganymede by analyzing the detected Lyman-α emissions. Molyneux et al. (2018) used observations obtained with the Cosmic Origins Spectrograph along with STIS data to characterize the variations in the emission and the composition of Ganymede's oxygen atmosphere on the leading and trailing sides from measured intensities at 1,304 and 1,356 Å. Very recently, Roth et al. (2021) found evidence of water vapor in Ganymede's atmosphere and found that near the subsolar point sublimated water vapor is more abundant than than molecular oxygen.

Various numerical simulations of Ganymede's magnetic field and plasma environment contribute to the understanding of its auroral emission. Kopp and Ip (2002) applied resistive magnetohydrodynamic (MHD) simulations to show that the open-closed field boundary (OCFB) is changing with respect to the varying magnetic environment around Ganymede. The OCFB marks the separatrix between those magnetic field lines of Ganymede that close on the moon and those that are connected to Ganymede on one end and to Jupiter on the other (Neubauer, 1998). Due to the magnetospheric plasma flow and the associated magnetic stresses, the OCFB on the upstream side is shifted to higher latitudes while it is dragged towards the equator on the downstream side. Jia et al. (2008) used single-fluid MHD simulations to describe the interaction of Ganymede's magnetosphere with the ambient magnetic field. Their findings indicate that the major process for plasma and energy to enter the magnetosphere is via magnetic reconnection which occurs on the down- and upstream sides, where ambient and intrinsic field lines are nearly anti-parallel. Reconnection primarily occurs at the magnetopause on the upstream side and in a thin equatorial region on the downstream side which extends several Ganymede radii away. The comparison between the observed location of Ganymede's peak auroral emission by McGrath et al. (2013) and MHD modeling of Ganymede's environment performed by Jia et al. (2008) showed that the locations of Ganymede's auroral ovals are well correlated with the OCFB of Ganymede's magnetic field lines. Duling et al. (2014)

Figure 1. Geometry of orbital direction, plasma flow and related terminology for the various hemispheres/sides of Ganymede. The plasma flow is faster than Ganymede's orbital velocity and therefore the trailing side is the upstream side of the plasma flow.

also modeled Ganymede's plasma interaction with an MHD model with a new description for the insulating boundary conditions on Ganymede's icy surface. The resultant location of the OCFB for various upstream conditions in Duling et al. (2014) and Jia et al. (2008) are very similar as discussed in Saur et al. (2015). Additionally, 3D multi-fluid MHD simulations were applied (Paty & Winglee, 2004, 2006) or hybrid models (Fatemi et al., 2016) were used to estimate neutral sputtering rates on the surface (Liuzzo et al., 2020). Further models focused on additional plasma effects of Ganymede's magnetosphere such as Hall MHD (Dorelli et al., 2015). Tóth et al. (2016) and Zhou et al. (2019, 2020) used embedded particle-cell and MHD models to better understand reconnection at Ganymede and the resultant energetic particle fluxes. For all these models, the structure and brightness of Ganymede's auroral bands, the subject of this work, are key observational constraints (next to Galileo in-situ measurements) to understand the physics of Ganymede's sub-Alfvénic mini-magnetosphere.

While a location map of the aurora was created by McGrath et al. (2013), and the time-variable aspects of Ganymede's aurora, as well as the local emission morphology was studied by Saur et al. (2015) and Musacchio et al. (2017), in this work we create a first complete global Mercator map of Ganymede's auroral brightness at OI 1,356 Å. Here we also use previously unpublished HST observations from 2017 to explicitly focus on the emission structure at the sub- and anti-Jovian flanks. We use the emissions at OI 1,356 Å because it provides the largest signal-to-noise ratio (SNR) compared to OI 1,304 Å (Musacchio et al., 2017). The brightness structure is analyzed with special regard to the continuity of both ovals. Our map will serve as a diagnostic tool for future studies of magnetospheric and auroral processes around Ganymede.

2. Observations and Data Processing

In this section, we describe the HST/STIS data sets which were used in our study. We also describe how we map auroral emission from Ganymede's disk onto a Mercator map.

2.1. Overview of the Observations

Six STIS campaigns were conducted during which Ganymede was observed in the FUV range between 1,150 and 1,700 Å. All observations were carried out with the G140L grating and used the Multi-Anode Micro-channel Array (MAMA) detector. Due to Ganymede's synchronized rotation around Jupiter, the various hemispheres are observable when Ganymede is at distinct elongations on its orbit. Table 1 lists the available programs and Figure 2 shows the distribution of Ganymede's elongation for the available data sets. For an impression of Ganymede's spatially varying emission morphology we display in Figure 3 selected observations at four different orbital positions ϕ_{orb}. They show Ganymede's leading, trailing, sub-Jovian and anti-Jovian side. On the leading and trailing side the ovals appear continuous across all visible longitudes, but on the sub-Jovian and the anti-Jovian side, the emission appears interrupted near 0° and 180° longitudes, respectively. Observations near 180° have not been presented before in the literature to the authors' knowledge. They give an impression that the auroral brightness is not continuous along all longitudes of Ganymede, which we will quantify further in Section 3.

For a complete map of the auroral emissions, all data sets of the HST/STIS campaigns in Table 1 were used to cover all available elongations of Ganymede's orbit. Ganymede was observed on the downstream side around 90° elongation during 30 exposures and on the upstream side near 270° during 10 exposures. Thus, of the 48 exposures, only 6 covered the sub- and anti-Jovian hemispheres. (Two additional exposures were distorted and unusable due to a guide-star failure.) Therefore, only six of the remaining 46 exposures covered the regions around 0° and 180° elongation.

Table 1
Available Programs Where Ganymede Was Observed With Hubble Space Telescope /Space Telescope Imaging Spectrograph (HST/STIS)

ID	Date	Orbit	Exposures ID	λ_{III} (°)	θ_{mag} (°)	λ_{obs} (°)	ϕ_{orb} (°)	Size (″)	Albedo (%)
7939	30 October 1998	1	o53k01010	229.7	8.32	1.86	288.05	1.71	2.2 ± 0.4
			o53k01020	239.7	7.39		288.67		
		2	o53k01030	276.3	2.38		290.82		
			o53k01040	291.8	−0.16		291.77		
		3	o53k01050	331.0	−6.13		294.22		
			o53k01060	345.6	−7.77		295.13		
		4	o53k01070	26.49	−9.45		297.62		
			o53k01080	39.52	−9.0		298.44		
8224	23 December 2000	1	o5d602010	263.8	4.31	3.09	102.99	1.75	1.9 ± 0.4
			o5d602020	272.8	2.93		103.54		
		2	o5d602030	308.6	−2.91		105.63		
			o5d602040	323.2	−5.09		106.53		
9296	30 November 2003	1	o8m301010	275.3	2.53	−1.38	335.36	1.33	1.8 ± 0.5
			o8m301020	285.1	0.94		335.95		
		2	o8m30103	322.5	−4.99		338.15		
			o8m301040	337.1	−6.86		339.04		
12244	19 November 2010	1	objy03010	174.3	8.50	2.12	99.42	1.64	1.9 ± 0.3
			objy03020	183.9	9.09		100.19		
		2	objy03030	218.6	9.04		102.81		
			objy03040	233.9	7.96		103.99		
		3	objy03050	273.2	2.87		106.94		
			objy03060	288.5	0.375		108.06		
	20 November 2010	4	objy03070	327.8	−5.72		110.86		
			objy03080	343.1	−7.52		111.93		
		5	objy03090	22.45	−9.5		114.61		
			objy030a0	37.75	−9.09		115.63		
	1 October 2011	1	objy11010	164.8	7.69	3.6	89.51	1.78	2.0 ± 0.3
			objy11020	174.5	8.52		90.10		
		2	objy11030	210.7	9.36		92.21		
			objy11040	226.1	8.59		93.15		
		3	objyb1010	272.7	2.94		96.12		
			objyb1020	282.4	1.38		96.71		
		4	objyb1030	319.8	−4.61		98.89		
			objyb1040	335.3	−6.66		99.84		
		5	objyb1050	14.89	−9.45		102.26		
			objyb1060	28.34	−9.42		103.08		

Table 1
Continued

ID	Date	Orbit	Exposures ID	λ_{III} (°)	θ_{mag} (°)	λ_{obs} (°)	ϕ_{orb} (°)	Size (″)	Albedo (%)
13328	23 January 2014	1	ocbug1010	145.2	5.36	1.77	78.90	1.7	1.5 ± 0.4
			ocbug1020	155.5	6.69		79.54		
		2	ocbui1010	307.9	−2.79		88.89		
			ocbui1020	318.2	−4.37		88.53		
	27 January 2014	3	ocbug2010	10.39	−9.34	1.77	270.22	1.58	2.1 ± 0.5
			ocbug2020	20.75	−9.5		270.86		
	25 February 2014	4	ocbuh3010	141.5	4.85	1.77	275.98	1.7	2.0 ± 0.5
			ocbuh3020	151.8	6.24		276.62		
14634	2 February 2017	1	od8k40010	197.2	9.48	−3.22	173.38	1.45	1.7 ± 0.3
		2	od8k40020	245.6	6.75		175.92		

Note. θ_{mag} is Ganymede's magnetic latitude in Jupiter's magnetosphere, λ_{obs} the sub-observer planetocentric latitude of HST and ϕ_{orb} the elongation of Ganymede around Jupiter as in Figure 2. Orbit refers to the number within a visit. Program 12244 consists of two visits with five orbits each taken approximately 1 year apart.

2.2. Processing Auroral Disk Images

The data analysis is performed with the flat-fielded detector counts from the `.flt` files (see STIS instrument handbook, Riley (2017)). The major tasks to generate individual disk images of Ganymede's auroral emissions include the determination of Ganymede's position, size and orientation on the detector and eliminating any solar-reflected and background emission photons which are superimposed on the data.
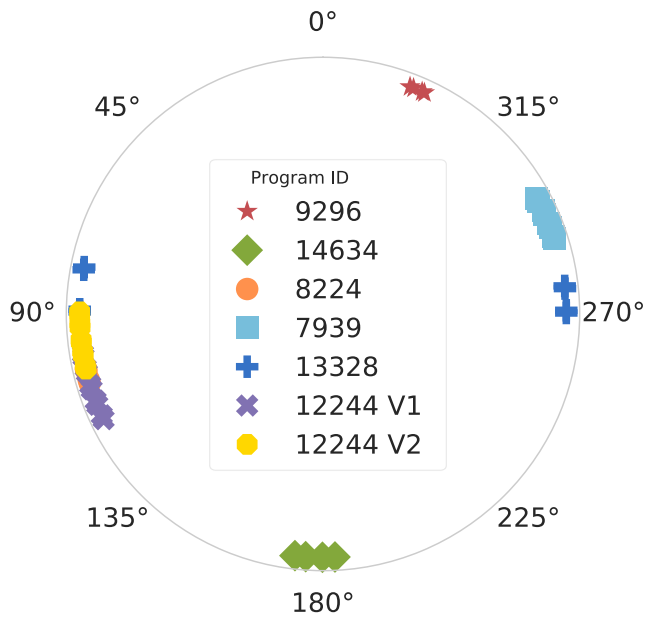
Using the SPICE tool-kit along with additional information provided in the scientific header of each file, we calculated the extension of Ganymede's disk and its tilt on the detector, the system-III longitude and magnetic latitude of Ganymede inside Jupiter's magnetic field, as well as Ganymede's elongation around Jupiter to determine the hemisphere observed in each exposure.

The size of Ganymede's disk on the detector varies between 53 to nearly 80 pixels depending on Ganymede's distance to Earth. Ganymede's exact position within the 2 arcsecond slit (corresponding to 82 pixels) needs to be determined from the observations. Therefore, we use the Lyman-α emission on the detector, which primarily consists of solar reflected light from Ganymede's surface and nearly spatially homogenous emission from the geocorona. The position of Ganymede is determined through a Gaussian fit along the direction of dispersion and along the direction of the slit. Due to a misalignment of the dispersion grating and the detector the y position of Ganymede $G_y(\lambda)$ is not constant along the dispersion axis. By performing Gaussian fits along the spatial axis inside the Lyman-α window and the spectral trace of the reflected solar light around 1,600–1,700 Å, we calculate two different y locations of the disk that are used to estimate $G_y(\lambda)$ by linearly interpolating between them.

To remove background emission in the form of dark pixels or interplanetary noise we apply previously used techniques (Roth, Saur, Retherford, Feldman, & Strobel, 2014; Roth, Saur, Retherford, Strobel, et al., 2014; Saur et al., 2015), in which the average detector counts at each wavelength (i.e., each pixel column) not affected by the signal from Ganymede are calculated and then subtracted from each pixel at that column. The solar reflected photons are removed by creating synthetic HST data sets which contain these reflected solar photons, similar to Musacchio et al. (2017). For each specific observation date the measured solar spectra $f_s(\lambda)$ are retrieved from data sets of the Upper Atmosphere Research Satellite for observations older than 2001, and from the Solar Extreme Ultraviolet Experiment installed on the Thermosphere Ionosphere Mesosphere Energetic and Dynamics orbiter for 2001 and later. Since the retrieved spectra are measured at the Sun-Earth distance d_{SE} they are rescaled to resemble the photons reflected by Ganymede's disk measured back at HST $f_{s,HST}(\lambda)$ by using

$$f_{s,HST}(\lambda) = a \cdot f_s(\lambda) \cdot \left(\frac{d_{SE}}{d_{SG} d_{GH}} \right)^2 R_G^2, \tag{1}$$

where d_{SG} and d_{GH} are the Sun-Ganymede distance and Ganymede-Hubble distance, respectively, and a the geometric albedo. From the reflected spectra, a synthetic HST image is created by superposing photon flux
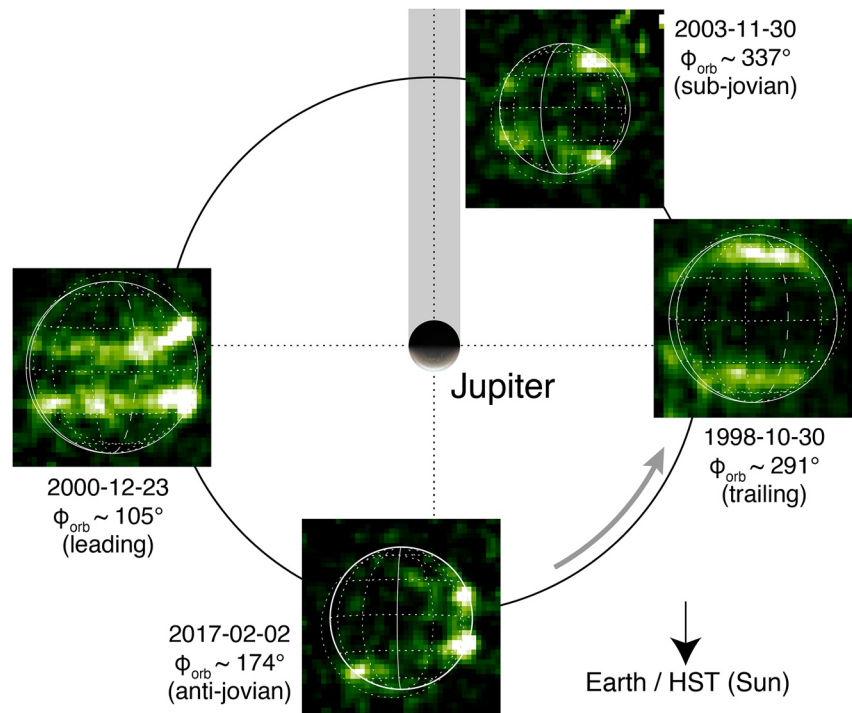
Figure 2. Overview of the elongation for all available exposures of each program, listed by their Program ID. Program 12244 consists out of two visits, which are displayed separately.

$f_{s,\mathrm{HST}}(\lambda)$ from uniformly reflecting disks for each wavelength. The resulting two-dimensional synthetic image is then convolved with the point spread function obtained by the *TinyTim* software tool (Krist et al., 2011). To match the unit of the synthetic data ϕ_{refl}, the measured detector counts C_{obs} are converted to photons cm^{-2} s^{-1} by dividing with the exposure time t and the effective HST primary mirror area A_{HST} of 45,238 cm^2, as given by
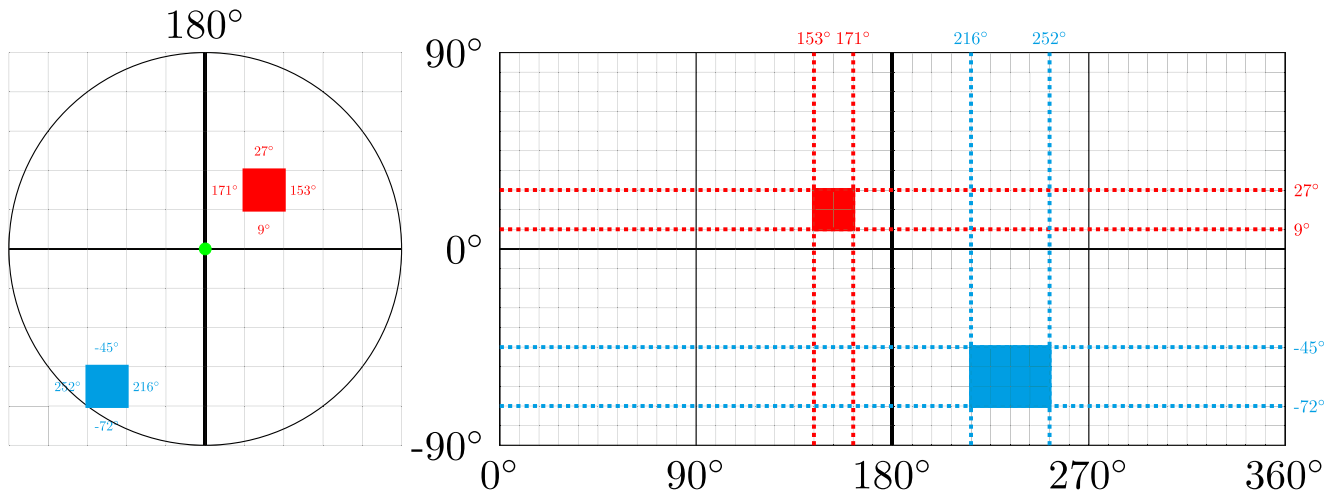
$$\phi_{\mathrm{obs}} = \frac{C_{\mathrm{obs}}}{t} \cdot \frac{1}{A_{\mathrm{HST}} \cdot T(\lambda)}. \qquad (2)$$

$T(\lambda)$ is the instrument dependent throughput that results in the conversion from measured detector counts to effective photons which reach the primary mirror. ϕ_{refl} and ϕ_{obs} are then transformed into the one dimensional spectral flux densities $s_{\mathrm{refl}}(\lambda)$ and $s_{\mathrm{obs}}(\lambda)$ in photons cm^{-2} s^{-1} Å^{-1} by the summation along the cross-dispersion axis of the detector. The geometric albedo a is then calculated by performing a least-square fit of s_{refl} to s_{meas} inside the wavelength window of 1,400 to 1,550 Å, where all detected emission is assumed to be due to solar reflected photons. The derived albedo values are listed in Table 1 and are in agreement with those discussed in the literature for the different hemispheres by, for example, Feldman et al. (2000), Saur et al. (2015), Musacchio et al. (2017), and Molyneux et al. (2020).

The effective spectral image ϕ_{eff} displaying only auroral emission that is free from background emissions and solar reflected photons from Ganymede's surface is calculated via

Figure 3. Selected observations of Ganymede's auroral emission at OI 1,356 Å showing Ganymede's leading, trailing, sub-Jovian, and anti-Jovian side. The auroral ovals are closer to the equator on the leading side compared to the trailing side, but appear continuous in both cases. In contrast, on the sub-Jovian and anti-Jovian side the aurora appears to be interrupted near 0° and 180° (meridians as solid white lines). The individual images of this Figure have been generated from the original HST data. The observations at the anti-Jovian geometry have not been published before, while observations at other orbital longitudes have already been displayed in the work discussed in Section 1.

Figure 4. Simplified illustration of how pixels are mapped from the processed disk array (left) to a Mercator map (right). The examples shows a disk viewed at central meridian of 180° west longitude. After calculating the latitudes and longitudes of each pixel edge, the Rayleigh values are inserted into the pixel corresponding to the respective region.

$$\phi_{\text{eff}} = \phi_{\text{obs}} - \phi_{\text{back}} - \phi_{\text{refl}}. \tag{3}$$

Before cropping the image to a 82×82 pixel sized array around Ganymede's disk at 1,356 Å and rotating it to align with the vertical axis, the image is converted into the unit Rayleigh (R) which is defined as a surface brightness with $1\ R = 10^6/4\pi$ photons cm^{-2} sr^{-1} s^{-1}, resulting in

$$R = \frac{4\pi}{10^6} \cdot \frac{\phi_{\text{eff}}}{m_s^2} \cdot \left(\frac{360 \cdot 3600}{2\pi} \right)^2. \tag{4}$$

Here, m_s is the plate scale of the FUV-MAMA detector with the G140L grating which is 0.0246 arcsec pixel^{-1} (Riley, 2017), and the last term represents conversion between arcsec and radian.

2.3. Creating the Auroral Map

From the final processed and rotated images a Mercator brightness map of the aurora is created by mapping the brightness value of each pixel lying on Ganymede's disk to a new position on an array which displays the range of 0°–360° west-longitude and −90° to +90° planetocentric latitude of Ganymede. The map is created as a 360×720 pixel array, resulting in a resolution of 0.5° per pixel in both longitudinal and latitudinal directions. After determining the area each pixel covers on Ganymede, the respective Rayleigh value is mapped to the corresponding region on the projected map as illustrated in Figure 4. The area that one pixel covers is calculated from the latitude and longitude of its pixel edges.

To determine the longitudinal and latitudinal positions of all pixels on the disk, they are first mapped on arcs of constant latitude. Because of the tilt of Ganymede as seen from the HST, the arcs are not straight lines but sections of ellipses. Pixels of the same latitude therefore are not necessarily in the same row. To infer the longitude of the pixel, the distance d from the center, that is, the sub-observer longitude $\varphi_{\text{sub−obs}}$, along the arc is compared to the length of the whole arc l. The longitude φ can then be calculated as $\varphi = \varphi_{\text{sub−obs}} + \arcsin(2\ d/l)$. Note that positions left from the center result in negative values of d, while positions right result in positive values. Since the tilt of Ganymede is small, the arcs can be assumed to cover 180° in longitude. Additionally we omitted sub-pixel discretization that would account for the variation of latitude and longitude along the pixel edges, but used the values of the pixel corners. Naturally, this translates every disk pixel to a rectified area on the Mercator map.

As the auroral emission is generated inside Ganymede's oxygen atmosphere the brightness measured can be affected by the position of a pixel on the disk. Due to the spherical extent of the atmosphere, photons registered by pixels near the edge of the disk can originate from a larger atmospheric column than those of the central pixel below the sub-observer point. To compensate for this effect, we scale the brightness measured by each pixel with

the atmospheric depth that lies inside the line-of-sight of that pixel as observed from HST. The newly shifted values then represent the brightness as observed from the zenith of each location which eliminates the distortion obtained from the viewpoint of HST. As 97% of Ganymede's oxygen atmosphere lies below an altitude of ~70 km (Marconi, 2007; Saur et al., 2015), we use a length of 70 km for the sub-observer atmospheric height H below the zenith. The value of each disk pixel R_{HST} is then adapted and shifted to the zenith via

$$R_Z(x, y) = R_{\text{HST}}(x, y) \cdot \frac{H}{L(x, y)}, \tag{5}$$

where L is the atmospheric length associated with each pixel as viewed from HST.

After creating individual Mercator maps for each set of HST observations, all individual 46 maps were combined into one complete map. To create the final map that contains all exposures, the mean Rayleigh brightness for one pixel x_m, y_m on the map is calculated from all Rayleigh values mapped to this pixel, weighted with the respective exposure time T, in the following way

$$\bar{R}(x_m, y_m) = \frac{\sum_i^N R_i(x_m, y_m) \cdot T_i}{\sum_i^N T_i}. \tag{6}$$

The averaged emission is weighted with exposure time to generate the best temporal averaged emission map in contrast to weighting with the inverse of the uncertainty squared, which would correspond to weighting with intensity. N is the number of exposures used for calculating the averaged brightness in a pixel on the mercator map. Performing this for all 360×720 pixels on the map creates the final brightness map of Ganymede's UV aurora at 1,356 Å.

From the Gaussian fits that were performed to locate Ganymede's disk on the detector, an uncertainty of ± 1 pixel is estimated for the deviation of Ganymede's central pixel. A deviation of one pixel could already resemble a significantly different location assigned to a pixel which is near the edge of the disk. We therefore only incorporate disk pixels into the map whose assigned locations lie within a defined window of uncertainty to assure a certain spatial accuracy of the map. For that, the uncertainty in latitudinal and longitudinal direction of each pixel is calculated for each exposure. The uncertainties Δx and Δy describe the total difference in latitude and longitude from both neighboring pixels of the mapped cell. Due to the spherical curvature, Δx and Δy are smaller at the disk's center and grow larger towards the edge. We therefore chose a threshold value to filter pixel for which the deviation of one cell would result in a larger spatial discrepancy. If any of the two uncertainties Δx or Δy exceeded a threshold of 15°, the corresponding pixel is not included into the map.

For additional evaluation tools, we use the same mapping procedure to map the total exposure time that went into each pixel on the Mercator map to assess the observational coverage of different regions on the map. Similarly we create a map for the SNR of each pixel on the Mercator map to identify the data quality for later interpretations. The SNR is calculated from the detector counts C, background emission counts B and solar reflected photons that are converted to detector counts S. These components are mapped into an individual map as previously described, but is unaffected by the atmospheric length correction and exposure time weighting. Since the total number of counts needs to be conserved, the counts are evenly re-distributed over all corresponding pixels on the map. The three individual maps for C, B, and S are then combined via
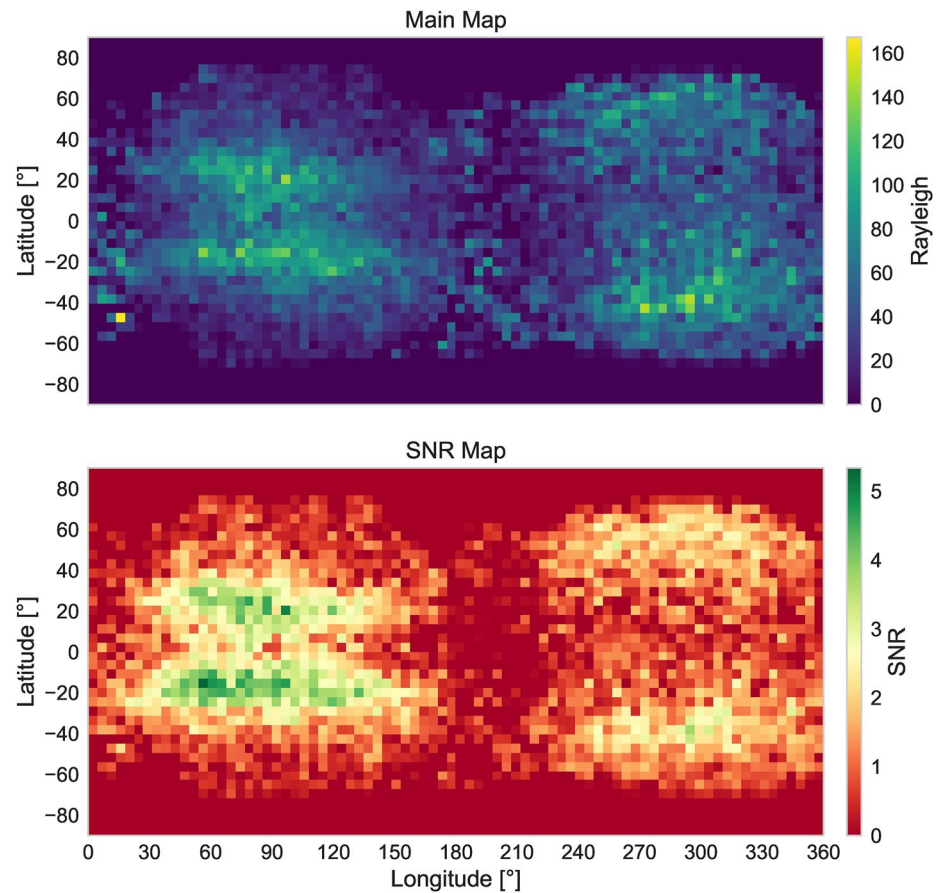
$$\text{SNR} = \frac{C - B - S}{\sqrt{C + B + S}}, \tag{7}$$

to create a complete SNR map.

3. Results

In this section, we present our calculated brightness map of Ganymede's auroral emission at 1,356 Å. We also analyze its properties and discuss the possible mechanisms responsible for its spatial structure.
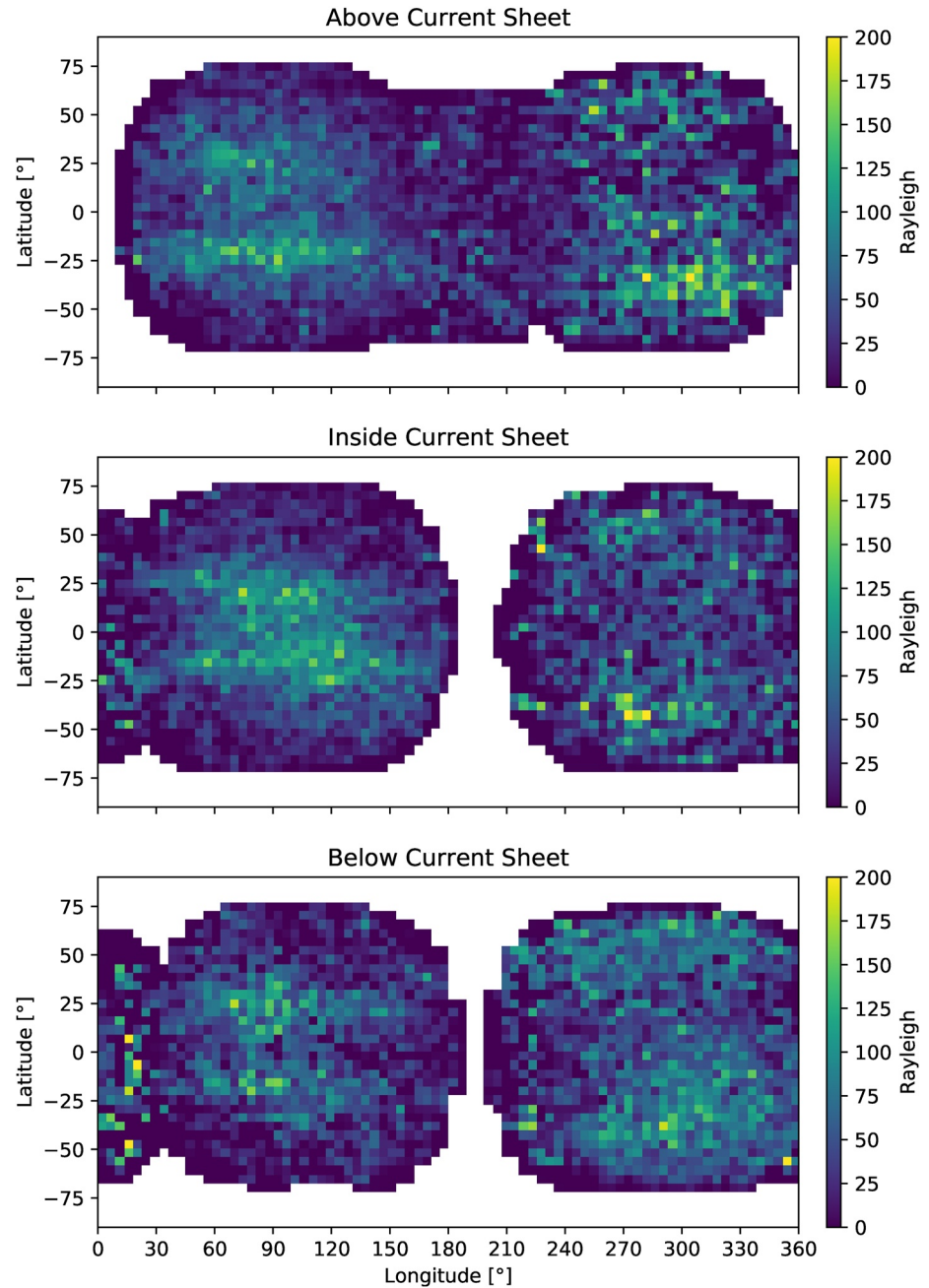
Figure 5. Main brightness map at 1,356 Å that incorporates all 46 exposures from Table 1 (top) and the corresponding signal-to-noise map (bottom).

3.1. Main Brightness Map

In Figure 5, we display the main, that is, averaged brightness map of Ganymede's aurora. The map was rebinned to cells which contain 9×9 pixel of the unbinned map in order to increase the SNR. The rebinned map therefore has a resolution of 40×80 pixel, where one pixel spans $4.5° \times 4.5°$ in latitude and longitude. From simple visual inspection of the brightness map, the auroral emission seems to be clearly dominant on the downstream and upstream hemispheres, while the transition regions appear noticeably fainter. The SNR map displayed in the bottom part of Figure 5 also represents this aspect to some extent as the SNRs are clearly higher on the upstream- and downstream sides, compared to the sub- and anti-Jovian longitudes around 0° and 180°, respectively. Note however that the SNR is large when the photon fluxes and/or the exposure times are large. With a total exposure of ~5,000–7,000 s for the sub- and anti-Jovian sides, the low SNR of ≤ 1 of individual pixels on the map indicate that very few photons could be detected at these longitudes.

3.2. Brightness Maps: Inside, Above and Below the Current Sheet

Figure 6 displays the brightness maps which were created when we separated the available exposures according to the magnetic latitude of Ganymede in Jupiter's magnetosphere. We choose as boundaries for the current sheet $\theta_{mag} = \pm 6°$ magnetic latitude. Thirteen exposures make up the map below the current sheet, 14 above the current sheet, and the remaining 19 exposures are used for the map where Ganymede is located within the current sheet. The maps show that the coverage of the main brightness map in Figure 5 is not evenly distributed for all magnetic latitudes. The longitudinal region between 180° and 210° is only covered by observations where Ganymede is above the current sheet. The comparison illustrates the prominent emission structures on the downstream and upstream sides, as well as the enhanced upstream emission on the southern oval across all three maps. Increased

Figure 6. Comparison of the evaluated 46 exposures separated by Ganymede's magnetic latitude when it is above ($\theta_{mag} > 6°$), inside ($|\theta_{mag}| \leq 6°$), or below ($\theta_{mag} < -6°$) the Jovian current sheet.

values around the 0° sub-Jovian longitude are only present in isolated pixels when Ganymede is below the current sheet and are not visible on the other two maps. They could be either a non-systematic, sporadic effect or an unknown systematic difference between northern and southern latitudes. However, the SNR map in Figure 5 shows that the fluxes of these pixels are barely significant due to the low exposure times and thus no firm conclusions can be reached.

3.3. Analysis of the Brightness Map

A global fit for the latitudes Θ of the ovals as a function of all longitude λ incorporating all exposures is generated in the form

Table 2
Fit Values for Equations (8) and (9)

Equations	Hemisphere	Θ_0	Θ_1	λ_1
(8)	North	32.3°	−16.9°	1.5°
(8)	South	−29.4°	11.6°	8.8°

Equations	Hemisphere	B_0	B_1	B_2	B_3	λ_1	λ_2	λ_3
(9)	North	46.2 R	9.4 R	28.2 R	5.2 R	19.9°	264.5°	236.1°
(9)	South	57.0 R	11.0 R	25.8 R	3.6 R	65.7°	237.4°	256.9°

$$\Theta(\lambda) = \Theta_0 + \Theta_1 \sin(\lambda + \lambda_1), \tag{8}$$

where λ is the western longitude and Θ_0, Θ_1, and λ_1 are the fitting parameter summarized in Table 2.

Average latitude values for the ovals are calculated inside the same longitude windows of 40°–150° and 240°–340° for both southern and northern emission. The windows are slightly off centered from 90° and 270° due to the shifted extrema (see Figure 7). The average latitudes on the downstream hemisphere of ±18.7° ± 4.5° as well as the mean upstream latitude of ±41.5° ± 6.7° are in accordance with the reported locations in McGrath et al. (2013).

To further compare our results with previous works, we first study the average positions of the northern and southern ovals when Ganymede is inside the current sheet and outside of it. Therefore we fit polynomials of second degree within downstream longitudes of 40°–150° and upstream longitudes of 240°–340° using a centroiding scheme as in Saur et al. (2015). The averaged latitudes are shifted by −5.4° ± 3.2° towards the equator on the downstream hemisphere when Ganymede is located inside the current sheet compared to outside. The retrieved shift of ±5.4° is in reasonable agreement with the shift of −4.1° ± 0.7° found in Musacchio et al. (2017). The detected shift by Musacchio et al. (2017) towards the poles on the upstream hemisphere is reproduced in our results only on the southern oval, and is not clearly observable on the northern oval location.
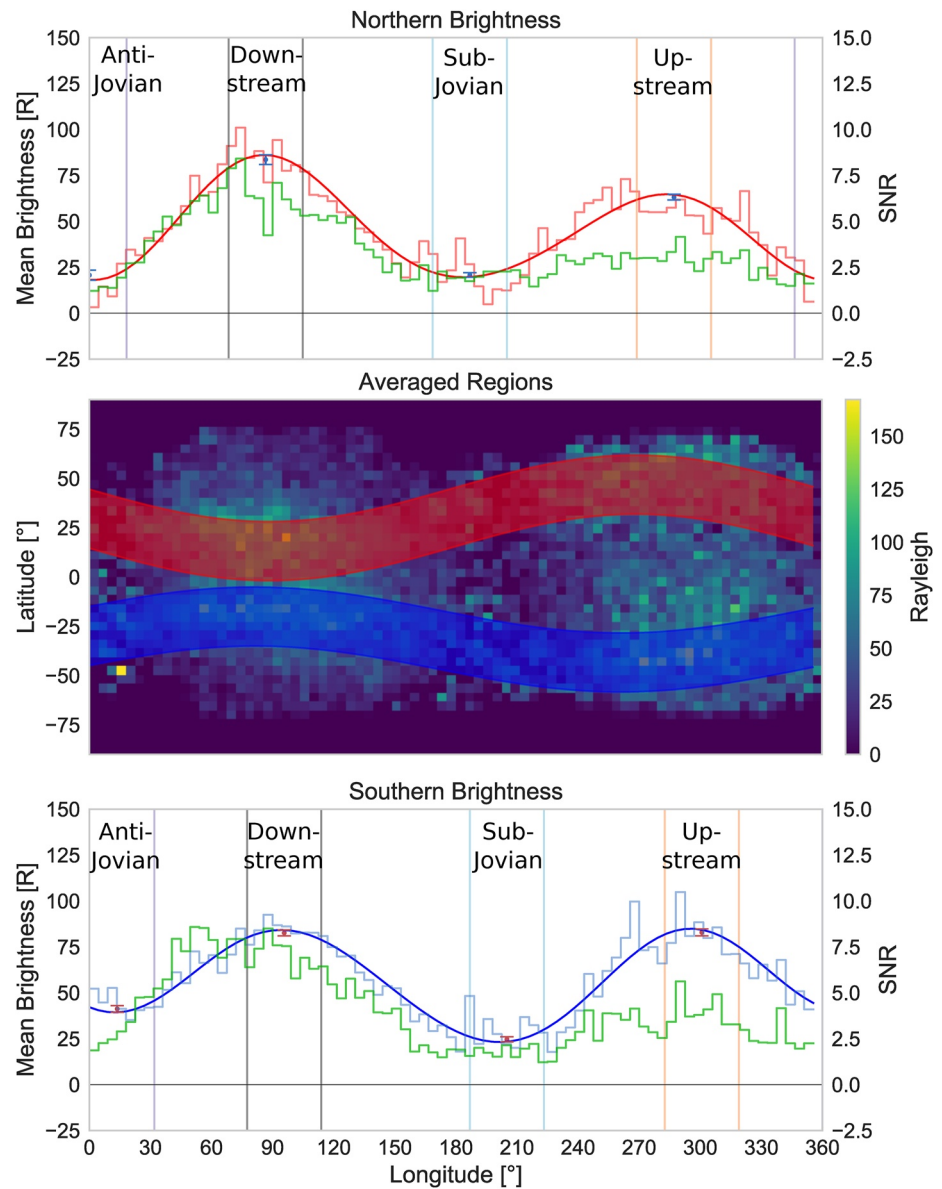
Combining all exposures, we calculate a disk averaged brightness and find values of 68.3 ± 8.9 R on the upstream and 90.5 ± 6.4 R on the downstream side. Comparing the auroral brightness from our maps when Ganymede is inside or outside of the current sheet, we find that the brightness on the downstream aurora increases by a factor of 1.3 ± 0.31 as Ganymede transitions into the current sheet and decreases by a factor of 0.78 ± 0.19 on the upstream side. Both values are well in agreement with the results of 1.33 ± 0.05 and 0.76 ± 0.07 by Musacchio et al. (2017).

To further characterize the emission structure of the northern and southern auroral emission, we fit the brightness within the bands displayed in Figure 7 in the form

$$B(\lambda) = B_0 + B_1 \sin(\lambda + \lambda_1) + B_2 \sin(2\lambda + \lambda_2) + B_3 \sin(3\lambda + \lambda_3) \tag{9}$$

with the fitting parameters B_0, B_1, B_2, B_3, λ_1, λ_2, and λ_3 provided in Table 2. The fit is based on the main map (Figure 5), where we used the brightness of bins at position $\Theta(\lambda)$ from Equation 8 plus its three latitudinally neighboring bins above and below. The latitudinal extension corresponds to approximately 31° and the associated band is highlighted on the map in Figure 7. With Equation 9, we introduce a fit function with 7 free parameters in order to resolve various asymmetries in the brightness distributions. The observed and fitted brightnesses are displayed in the top and bottom panels of Figure 7 along with the integrated SNR of those regions in green. For both the northern and southern ovals, the averaged brightness exhibits a sinusoidal shape without abrupt drops or cut-offs, which can also be observed in the SNR. From the brightest peaks on the down- and upstream sides, the brightness steadily decreases towards ∼0° and ∼180° longitudes regions where they reach their lowest values.

To quantify the brightness change along the ovals we average the brightness inside windows of 36° longitude around the fitted brightest and faintest points along the sinusoidal fits. The widths of these windows were chosen such that enough data points lead to a robust value and that the widths are still narrow enough such that the

Figure 7. Average auroral brightness (based on all available exposures) for the northern (top, red) and southern (bottom, blue) ovals as a function of longitude. The average brightness is approximated by sinusoidal based fit functions (also red and blue). The signal-to-noise ratio for the averaged regions is plotted in green. The center panel is a replot of the main brightness map (Figure 5) and includes as red and blue bands the oval regions used to calculate the values in the top and bottom panel (more details see Section 3.3). Regions with a width of 36° longitude used to calculate average peak and faintest emission are indicated by vertical bars in the top and bottom panels, and the points with error bars indicate average values in these longitude ranges (Table 3).

minimum and maximum are approximated well. The uncertainties for those values is calculated from the variance of the brightness inside those 36° windows.

Average brightness values within various longitudinal regions are quantitatively provided in Table 3. The values are calculated as algebraic averages within a band given by the bin with the maximum brightness ±3 bin in latitudinal direction and within the longitude ranges specified in the table. The area for each region is approximately 36° × 31°. Within the northern oval, the emission decreases from 83.8 ± 2.6 R on the downstream side and 63.5 ± 1.6 R on the upstream side to small values of 19.6 ± 2.8 and 20.3 ± 1.3 R on the sub- and anti-Jovian longitudes, respectively. The emission on the flanks (i.e., Jovian and anti-Jovian sides) is therefore a factor of 3.7 ± 0.4 fainter than on the up- and downstream sides. For the southern oval, the upstream and downstream

Table 3
Averaged Brightness Within Various Longitudinal Ranges and Their Ratios

		Downstream/upstream		Jovian side/anti-Jovian side		Ratios
Northern	Longitude range	68°–105°	269°–305°	346°–18°	168°–205°	
	Brightness within range	83.8 ± 2.6 R	63.5 ± 1.6 R	19.6 ± 2.8 R	20.3 ± 1.3 R	
	Joint brightness	73.7 ± 1.5 R		19.9 ± 1.5 R		3.7 ± 0.4
Southern	Longitude range	77°–114°	283°–319°	0°–32°	187°–223°	
	Brightness within range	82.7 ± 1.6	83.0 ± 1.9 R	40.9 ± 1.8	24.5 ± 1.4 R	
	Joint brightness	82.9 ± 1.2 R		32.7 ± 1.1 R		2.5 ± 0.2
North-south average		78.3 ± 1.0 R		26.3 ± 0.9 R		3.0 ± 0.1

Note. Brightness is given in units of Rayleigh (*R*). See text for details on averaging. Downstream/upstream and sub-Jovian/anti-Jovian averages are referred to as joint brightnesses, respectively. They are provided together with the north-south averages for a basic overview.

brightness is similar with an average value of 82.9 ± 1.2 R. The average faint emission around 0° and 180° is significantly stronger on the southern oval with an averaged brightness of 32.7 ± 1.1 R compared to the northern hemisphere. While the decrease towards the sub-Jovian hemisphere is only a factor of 2.0 ± 0.1, where the emission is still 40.9 ± 1.8 R, the brightness decreases by a factor of 3.5 ± 0.2 towards the anti-Jovian longitude where the auroral brightness is only 24.5 ± 1.4 R. For the southern oval, we find an average brightness change by a factor of 2.5 ± 0.2 when comparing the averages of the trailing and leading sides to the flanks. Finally, combining the emission from the northern and the southern ovals within the individual longitudes given in Table 3, we find the emission on the flanks is a factor of 3.0 ± 0.1 lower compared to the average oval brightness of the upstream and downstream side.
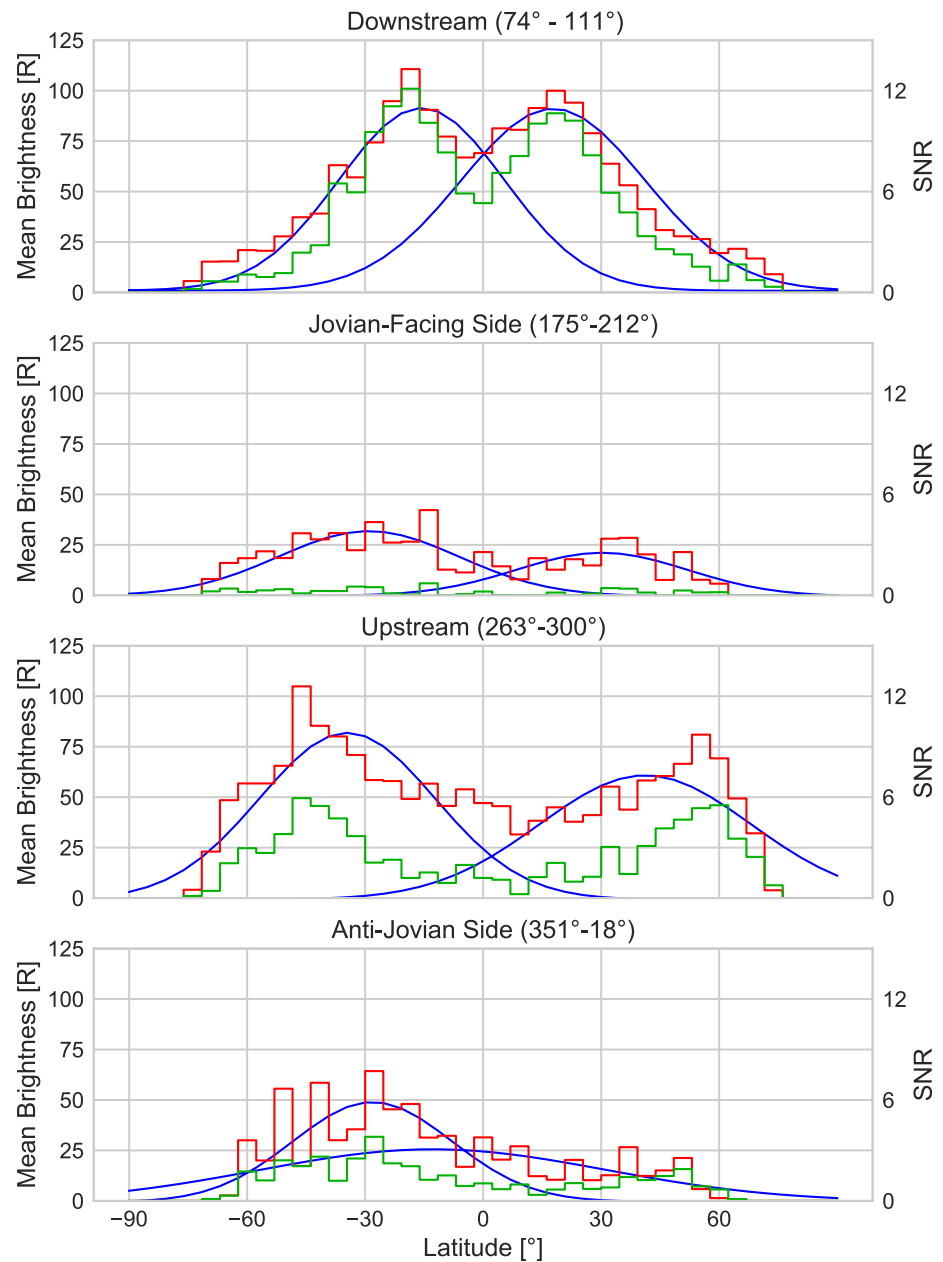
The main map in Figure 5 shows that the maximum brightness is not exactly located at 90° and 270° longitudes, that is, symmetric with respect to the Jovian and anti-Jovian side. On the downstream side the maximum is at 85° for the northern band and at 95° for the southern band. On the upstream side the emission maxima lie at 283° for the northern band and at 297° for the southern band, that is, maximum brightness is shifted towards the Jovian-facing side by approximate 20° on average. The reason for this asymmetry could lie in the slightly tilted magnetic moment of Ganymede (Kivelson et al., 2002) and/or in asymmetries of the plasma interaction, for example, due to the Hall effect (Dorelli et al., 2015; Saur et al., 1999).

On the anti-Jovian flank, brighter regions appear to be present around longitude 190°, in both the northern and the southern regions, embedded inside the faint aurora. They also appear inside the brightness curves in the top and bottom panels of Figure 7. The peaks are not correlated with a similar increase in the SNR due to low total exposure times covering this region. Therefore, it is doubtful if the locally enhanced brightness patches are physically real.

For several reasons, the largest values within our auroral brightness map are smaller than previously reported values in the range of 100 R up to 300 R in locally bright areas in Feldman et al. (2000). For one we retrieved the values from our auroral map instead of the observed disks. Since the map incorporates multiple exposures into a weighted average of each pixel on the map, any individual high-count emission from a detector pixel of one exposure gets averaged by exposures which went into the same map pixel with fewer detected counts. Additionally, unlike studies where the observed disks were evaluated, we accounted for the atmospheric line-of-sight effect described in Section 2.3 when creating the map. Thus, high brightness pixels near the edges of the disk are given a lower adapted-brightness on our map. Lastly, the rebinning of our map to increase the SNR value affects the brightness as it averages individual bright spots. Since the actual size chosen to rebin has a direct impact on the brightness averaging, our size of 3 × 3 pixel used for rebinning exceeds the rebinning size of 2 × 2 used McGrath et al. (2013) on the disks.

3.4. Interpretation of the Auroral Brightness Map

There are different hypotheses on the cause of Ganymede's aurora and therefore there are also different ways to interpret the derived brightness maps of Ganymede's aurora in Figure 5. To point out different possible

Figure 8. Mean brightness as function of latitude for the downstream, Jovian-facing side, the upstream side and the anti-Jovian side (in red). For the mean brightness, latitudinal bands within a width of three bins have been used. The curves in green display the associated SNR. In blue, a Gaussian fit to the mean brightness within the northern and southern hemispheres is overlaid.

interpretations, we display the UV brightness as a function of latitude in Figure 8 for the upstream, the downstream and the sub- and anti-Jovian sides, respectively. For the upstream and downstream sides a similar analysis has been performed by Musacchio et al. (2017). On the upstream and downstream sides the brightness has two maxima, respectively, consistent with the existence of two auroral bands in the north and south. We display these structures by separately fitting Gaussians on the northern and southern hemisphere, respectively (shown as blue lines in Figure 8). The brightness maxima are closer to the equator on the downstream side compared to the upstream side due to the magnetic stresses of Jupiter's magnetosphere on Ganymede's magnetic field and plasma environment. The downstream aurora is also brighter on average compared to the upstream side.

The brightness distribution as a function of latitude on the Jupiter facing side and the anti-Jupiter side shown in Figure 8 is less clearly structured. The Jovian-facing side has two modest maxima in the northern and southern hemispheres with slightly reduced values around the equator. The anti-Jovian facing side shows a modest maximum only in the south. Emission from latitudes larger than $\pm70°$ latitudes are difficult to assess due to the viewing geometry from Earth.

Auroral emission displayed in Figures 5 and 8 maximizes within upstream and downstream northern and southern crescents away from the equator. But auroral emission with a smaller amplitude is still present within all other longitudes. Several possible scenarios causing the auroral emission pattern are possible.

1. One possibility is that reconnection near the open-closed field line boundary generates energized particles which propagate along the field lines and generates northern and southern auroral crescents on the upstream and downstream side, respectively. Maximum reconnection is expected to occur based on numerical simulations and theory on the upstream and downstream side (Duling et al., 2014; Neubauer, 1998; Tóth et al., 2016; Zhou et al., 2019). Consequently the reconnection intensity gets weaker towards the flanks of the sub- and anti-Jovian hemisphere, where the plasma flow is parallel to the magnetopause and the exerted ram pressure diminishes. Energetic particles will however drift perpendicular to the field lines and might be scattered and thus additionally diffuse across the field lines to generate auroral emission on field lines located away from the reconnection sites. This could be a scenario explaining the non-negligible, but weak emission on the flanks compared to the upstream and downstream side and the weak emission near equatorial latitudes.

2. Alternatively, several different auroral generator mechanisms could contribute to Ganymede's auroral emission. Next to reconnection on the upstream and downstream side, shear flow near the OCFB could drive an electric current system with field-aligned electric current predominately towards and away from Ganymede's ionosphere on the flanks (e.g., Jia et al., 2009). These currents might drive parallel electric fields which accelerate particles subsequently creating the aurora (Eviatar et al., 2001). The existence and nature of such DC parallel electric fields similar to observations and theory from Earth (Knight, 1973) is however uncertain at Ganymede. Within the closed-field region of Ganymede's magnetosphere, possible MHD and plasma waves could be subject to wave-particle interaction and thus produce energetic particles (e.g., Eviatar et al., 2001; Lysak & Lotko, 1996; Saur et al., 2018). Additionally, on open field lines, energetic ions and electrons from Jupiter's magnetosphere will contribute to Ganymede's polar cap auroral emission. Several of these processes thus could jointly shape Ganymede's auroral structure.

3. A third possibilty contributing to the auroral emission pattern is a spatially variable neutral atmosphere. The primary component of Ganymede's atmosphere is O_2 with a contribution from H_2O near the sub-solar point (Hall et al., 1998; Marconi, 2007; Roth et al., 2021). The spatial variability and composition of the atmosphere has been modeled by, for example, Collinson et al. (2018); Leblanc et al. (2017); Carnielli et al. (2019); Plainaki et al. (2020). The atmosphere's O_2 component is however expected to only weakly vary across the surface of Ganymede because O_2 does not freeze out on the surface (e.g., Strobel, 2005). The spatial variability of other neutral components is expected to more strongly contribute to the spatial variability of Ganymede's UV emission.

4. Summary

In this work, we used a set of 46 exposures taken with the STIS instrument of the HST from 1998 to 2017 to create a global brightness map of Ganymede's auroral emission at 1,356 Å. Our results are consistent with the location map of McGrath et al. (2013) and the brightness values derived in Musacchio et al. (2017). The map and analysis of this work shows that the brightness of Ganymede's aurora varies strongly with longitude. With strongest emission on the upstream and downstream sides around 90° and 270° longitude, the emission around the sub- and anti-Jovian longitudes near 0° and 180° are on average 3.0 times fainter. While the brightness does not completely vanish, thus making the aurora not strictly discontinuous, the northern and southern emission can each be characterized to consist of two dominant auroral crescents rather than a continuous oval. Compared to other celestial bodies in our solar system which exhibit auroral emission like Earth, Jupiter, Saturn and Uranus (e.g., Bhardwaj & Gladstone, 2000; Clarke et al., 2005; Lamy et al., 2012) the distinctively cresent-shaped contributions to its auroral ovals makes Ganymede aurora unique in the solar system.

This study presents new observational constraints on Ganymede's auroral ovals. The derived auroral maps can be considered also maps of Ganymede's magnetospheric physics, which will be helpful for future investigations of Ganymede's mini-magnetosphere and its auroral acceleration processes. For example, it will be interesting to relate the spatial distribution of the auroral emission to the in-situ magnetic field and plasma measurements by the Galileo spacecraft (e.g., Collinson et al., 2018; Eviatar et al., 2000; Kivelson et al., 2002). They will be useful for a comprehensive understanding of Ganymede and for the planing of future measurements taken by the JUICE spacecraft (Grasset et al., 2013) and for interpretation of observation by the Juno spacecraft (Bolton et al., 2017). These observations will help to provide an in depth understanding of Ganymede's magnetosphere and internal structure, but also its coupling to Jupiter (Bonfond et al., 2017) and its influence of Jupiter's magnetosphere. The sub-Alfvénic aurora of Ganymede—the only sub-Alfvénic one in the solar system—might also be a model case for sub-Alfvénic aurora on close-in exoplanets (e.g., Saur et al., 2013, 2021; Zarka, 2007).

Data Availability Statement

All data used in this study is available on the Mikulski Archive for Space Telescopes of the Space Telescope Science Institute at http://archive.stsci.edu/hst/. The specific data sets used here are listed in Table 1 and can be accessed at: Moos (1997), McGrath (1999), Ford (2002), Saur (2010), Nichols (2013), and Grodent (2016). The data for Figures 5–8 can be accessed at Marzok et al. (2022).

References

Alday, J., Roth, L., Ivchenko, N., Retherford, K. D., Becker, T. M., Molyneux, P., & Saur, J. (2017). New constraints on Ganymede's hydrogen corona: Analysis of Lyman-α emissions observed by HST/STIS between 1998 and 2014. *Planetary and Space Science*, *148*, 35–44. https://doi.org/10.1016/j.pss.2017.10.006

Bhardwaj, A., & Gladstone, G. R. (2000). Auroral emissions of the giant planets. *Review of Geophysics*, *38*(3), 295–353. https://doi.org/10.1029/1998rg000046

Bolton, S. J., Lunine, J., Stevenson, D., Connerney, J. E. P., Levin, S., Owen, T. C., et al. (2017). The Juno mission. *Space Science Reviews*, *213*(1–4), 5–37. https://doi.org/10.1007/s11214-017-0429-6

Bonfond, B., Grodent, D., Badman, S. V., Saur, J., Gérard, J.-C., & Radioti, A. (2017). Similarity of the Jovian satellite footprints: Spots multiplicity and dynamics. *Icarus*, *292*, 208–217. https://doi.org/10.1016/j.icarus.2017.01.009

Carnielli, G., Galand, M., Leblanc, F., Leclercq, L., Modolo, R., Beth, A., et al. (2019). First 3D test particle model of Ganymede's ionosphere. *Icarus*, *330*, 42–59. https://doi.org/10.1016/j.icarus.2019.04.016

Clarke, J. T., Gérard, J.-C., Grodent, D., Wannawichian, S., Gustin, J., Connerney, J., et al. (2005). Morphological differences between Saturn's ultraviolet aurorae and those of Earth and Jupiter. *Nature*, *433*(7027), 717–719. https://doi.org/10.1038/nature03331

Collinson, G., Paterson, W. R., Bard, C., Dorelli, J., Glocer, A., Sarantos, M., & Wilson, R. (2018). New results from Galileo's first flyby of Ganymede: Reconnection-driven flows at the low-latitude magnetopause boundary, crossing the cusp, and icy ionospheric escape. *Geophysical Research Letters*, *45*(8), 3382–3392. https://doi.org/10.1002/2017GL075487

Dorelli, J. C., Glocer, A., Collinson, G., & Tóth, G. (2015). The role of the Hall effect in the global structure and dynamics of planetary magnetospheres: Ganymede as a case study. *Journal of Geophysical Research: Space Physics*, *120*(7), 5377–5392. https://doi.org/10.1002/2014JA020951

Duling, S., Saur, J., & Wicht, J. (2014). Consistent boundary conditions at nonconducting surfaces of planetary bodies: Applications in a new Ganymede MHD model. *Journal of Geophysical Research: Space Physics*, *119*(6), 4412–4440. https://doi.org/10.1002/2013JA019554

Eviatar, A., Strobel, D. F., Wolfven, B. C., Feldman, P., McGrath, M. A., & Williams, D. J. (2001). Excitation of the Ganymede ultraviolet aurora. *The Astrophysical Journal*, *555*(2), 1013–1019. https://doi.org/10.1086/321510

Eviatar, A., Williams, D. J., Paranicas, C., McEntire, R. W., Mauk, B. H., & Kivelson, M. G. (2000). Trapped energetic electrons in the magnetosphere of Ganymede. *Journal of Geophysical Research*, *105*(A3), 5547–5554. https://doi.org/10.1029/1999JA900450

Fatemi, S., Poppe, A. R., Khurana, K. K., Holmström, M., & Delory, G. T. (2016). On the formation of Ganymede's surface brightness asymmetries: Kinetic simulations of Ganymede's magnetosphere. *Geophysical Research Letters*, *43*(10), 4745–4754. https://doi.org/10.1002/2016GL068363

Feldman, P. D., McGrath, M. A., Strobel, D. F., Moos, H. W., Retherford, K. D., & Wolven, B. C. (2000). HST/STIS ultraviolet imaging of polar aurora on Ganymede. *The Astrophysical Journal*, *555*(2), 1085–1090. https://doi.org/10.1086/308889

Ford, H. (2002). *Jovian satellites*. HST Proposal. Retrieved from https://archive.stsci.edu/proposal_search.php?mission=hst&id=9296

Grasset, O., Dougherty, M. K., Coustenis, A., Bunce, E. J., Erd, C., Titov, D., et al. (2013). JUpiter ICy moons Explorer (JUICE): An ESA mission to orbit Ganymede and to characterise the Jupiter system. *Planetary and Space Science*, *78*, 1–21. https://doi.org/10.1016/j.pss.2012.12.002

Grodent, D. C. (2016). *HST-Juno synergistic approach of Jupiter's magnetosphere and ultraviolet auroras*. HST Proposal. Retrieved from https://archive.stsci.edu/proposal_search.php?id=14634&mission=hst

Hall, D. T., Feldman, P. D., McGrath, M. A., & Strobel, D. F. (1998). The far-ultraviolet oxygen airglow of Europa and Ganymede. *The Astrophysical Journal*, *499*(5), 475–481. https://doi.org/10.1086/305604

Jia, X., Walker, R., Kivelson, M., Khurana, K., & Linker, J. (2008). Three-dimensional MHD simulations of Ganymede's magnetosphere. *Journal of Geophysical Research*, *113*(A6), A06212. https://doi.org/10.1029/2007ja012748

Jia, X., Walker, R., Kivelson, M., Khurana, K., & Linker, J. (2009). Properties of Ganymede's magnetosphere inferred from improved three-dimensional MHD simulations. *Journal of Geophysical Research*, *114*(A9), A09209. https://doi.org/10.1029/2009JA014375

Kivelson, M. G., Khurana, K. K., & Volwerk, M. (2002). The permanent and inductive magnetic moments of Ganymede. *Icarus*, *157*(2), 507–522. https://doi.org/10.1006/icar.2002.6834

Kivelson, M. G., Khurana, K. K., Walker, R. J., Russell, C. T., Linker, J. A., Southwood, D. J., & Polanskey, C. (1996). A magnetic signature at Io: Initial report from the Galileo magnetometer. *Science*, *273*(5273), 337–340. https://doi.org/10.1126/science.273.5273.337

Knight, S. (1973). Parallel electric fields. *Planetary and Space Science*, *21*(5), 741–750. https://doi.org/10.1016/0032-0633(73)90093-7

Kopp, A., & Ip, W. (2002). Resistive MHD simulations of Ganymede's magnetosphere: 1. Time variabilities of the magnetic field topology. *Journal of Geophysical Research*, *107*, SMP-41. https://doi.org/10.1029/2001ja005071

Krist, J. E., Hook, R. N., & Stoehr, F. (2011). 20 years of Hubble Space Telescope optical modeling using tiny tim. In *Society of Photo-Optical Instrumentation Engineers (SPIE) Conference Series* (Vol. 8127). https://doi.org/10.1117/12.892762

Lamy, L., Prangé, R., Hansen, K. C., Clarke, J. T., Zarka, P., Cecconi, B., et al. (2012). Earth-based detection of Uranus' aurorae. *Geophysical Research Letters*, *39*(7), L07105. https://doi.org/10.1029/2012GL051312

Leblanc, F., Oza, A. V., Leclercq, L., Schmidt, C., Cassidy, T., Modolo, R., et al. (2017). On the orbital variability of Ganymede's atmosphere. *Icarus*, *293*, 185–198. https://doi.org/10.1016/j.icarus.2017.04.025

Liuzzo, L., Poppe, A. R., Paranicas, C., Nénon, Q., Fatemi, S., & Simon, S. (2020). Variability in the energetic electron bombardment of Ganymede. *Journal of Geophysical Research: Space Physics*, *125*(9), e28347. https://doi.org/10.1029/2020JA028347

Lysak, R. L., & Lotko, W. (1996). On the kinetic dispersion relation for shear Alfvén waves. *Journal of Geophysical Research*, *101*(A3), 5085–5094. https://doi.org/10.1029/95ja03712

Marconi, M. L. (2007). A kinetic model of Ganymede's atmosphere. *Icarus*, *190*(1), 155–174. https://doi.org/10.1016/j.icarus.2007.02.016

Marzok, A., Schlegel, S., Saur, J., Roth, L., Grodent, D., Strobel, D. F., & Retherford, K. D. (2022). *Figure data for "Mapping the brightness of Ganymede's ultraviolet aurora using Hubble Space Telescope observations"*. Zenodo. https://doi.org/10.5281/zenodo.6564687

McGrath, M. (1999). *UV imaging of Europa & Ganymede: Unveiling satellite aurora & electrodynamical interactions*. HST Proposal. Retrieved from https://archive.stsci.edu/proposal_search.php?mission=hst&id=8224

McGrath, M. A., Jia, X., Retherford, K. D., Feldman, P. D., Strobel, D. F., & Saur, J. (2013). Aurora on Ganymede. *Journal of Geophysical Research: Space Physics*, *118*(5), 2043–2054. https://doi.org/10.1002/jgra.50122

Molyneux, P. M., Nichols, J. D., Bannister, N. P., Bunce, E. J., Clarke, J. T., Cowley, S. W. H., et al. (2018). Hubble Space Telescope observations of variations in Ganymede's oxygen atmosphere and aurora. *Journal of Geophysical Research: Space Physics*, *123*(5), 3777–3793. https://doi.org/10.1029/2018JA025243

Molyneux, P. M., Nichols, J. D., Becker, T. M., Raut, U., & Retherford, K. D. (2020). Ganymede's far-ultraviolet reflectance: Constraining impurities in the surface ice. *Journal of Geophysical Research: Planets*, *125*(9), e06476. https://doi.org/10.1029/2020JE006476

Moos, H. (1997). *STIS determination of OI emissions from Ganymede*. HST Proposal. Retrieved from https://archive.stsci.edu/proposal_search.php?id=7939&mission=hst

Musacchio, F., Saur, J., Roth, L., Retherford, K. D., McGrath, M. A., Feldman, P. D., & Strobel, D. F. (2017). Morphology of Ganymede's FUV auroral ovals. *Journal of Geophysical Research: Space Physics*, *122*(3), 2855–2876. https://doi.org/10.1002/2016JA023220

Neubauer, F. M. (1998). The sub-Alfvénic interaction of the Galilean satellites with the Jovian magnetosphere. *Journal of Geophysical Research*, *103*(E9), 19843–19866. https://doi.org/10.1029/97je03370

Nichols, J. (2013). *Observing Ganymede's atmosphere and auroras with COS and STIS. HST Proposal*. Retrieved from https://archive.stsci.edu/proposal_search.php?mission=hst&id=13328

Paty, C., & Winglee, R. (2004). Multi-fluid simulations of Ganymede's magnetosphere. *Geophysical Research Letters*, *31*(24), L24806. https://doi.org/10.1029/2004gl021220

Paty, C., & Winglee, R. (2006). The role of ion cyclotron motion at Ganymde: Magnetic morphology and magnetospheric dynamics. *Geophysical Research Letters*, *33*(10), L10106. https://doi.org/10.1029/2005gl025273

Plainaki, C., Massetti, S., Jia, X., Mura, A., Milillo, A., Grassi, D., et al. (2020). Kinetic simulations of the Jovian energetic ion circulation around Ganymede. *The Astrophysical Journal*, *900*(1), 74. https://doi.org/10.3847/1538-4357/aba94c

Riley, A. (2017). *STIS Instrument Handbook* (Version 16.0). STScI.

Roth, L., Ivchenko, N., Gladstone, G. R., Saur, J., Grodent, D., Bonfond, B., et al. (2021). A sublimated water atmosphere on Ganymede detected from Hubble Space Telescope observations. *Nature Astronomy*, *5*(10), 1043–1051. https://doi.org/10.1038/s41550-021-01426-9

Roth, L., Saur, J., Retherford, K. D., Feldman, P. D., & Strobel, D. F. (2014). A phenomenological model of Io's UV aurora based on HST/STIS observations. *Icarus*, *228*, 386–406. https://doi.org/10.1016/j.icarus.2013.10.009

Roth, L., Saur, J., Retherford, K. D., Strobel, D. F., Feldman, P. D., McGrath, M. A., & Nimmo, F. (2014). Transient water vapor at Europa's south pole. *Science*, *343*(6167), 171–174. https://doi.org/10.1126/science.1247051

Saur, J. (2010). *Mapping Ganymede's time variable aurora in the search for a subsurface ocean*. HST Proposal. Retrieved from https://archive.stsci.edu/proposal_search.php?mission=hst&id=12244

Saur, J., Duling, S., Roth, L., Jia, X., Strobel, D. F., Feldman, P. D., et al. (2015). The search for a subsurface ocean in Ganymede with Hubble Space Telescope observations of its auroral ovals. *Journal of Geophysical Research: Space Physics*, *120*(3), 1715–1737. https://doi.org/10.1002/2014JA020778

Saur, J., Grambusch, T., Duling, S., Neubauer, F. M., & Simon, S. (2013). Magnetic energy fluxes in sub-Alfvénic planet star and moon planet interactions. *Astronomy & Astrophysics*, *552*, A119. https://doi.org/10.1051/0004-6361/201118179

Saur, J., Janser, S., Schreiner, A., Clark, G., Mauk, B. H., Kollmann, P., et al. (2018). Wave-particle interaction of Alfvén waves in Jupiter's magnetosphere: Auroral and magnetospheric particle acceleration. *Journal of Geophysical Research: Space Physics*, *123*(11), 9560–9573. https://doi.org/10.1029/2018JA025948

Saur, J., Neubauer, F. M., Strobel, D. F., & Summers, M. E. (1999). Three-dimensional plasma simulation of Io's interaction with the Io plasma torus: Asymmetric plasma flow. *Journal of Geophysical Research*, *104*(A11), 25105–25126. https://doi.org/10.1029/1999ja900304

Saur, J., Willmes, C., Fischer, C., Wennmacher, A., Roth, L., Youngblood, A., et al. (2021). Brown dwarfs as ideal candidates for detecting UV aurora outside the Solar System: Hubble Space Telescope observations of 2MASS J1237+6526. *Astronomy & Astrophysics*, *655*, A75. https://doi.org/10.1051/0004-6361/202040230

Strobel, D. F. (2005). Comparative planetary atmospheres of the Galilean satellites. *Highlights of Astronomy*, *13*, 894–895. https://doi.org/10.1017/s1539299600017433

Tóth, G., Jia, X., Markidis, S., Peng, I. B., Chen, Y., Daldorff, L. K. S., et al. (2016). Extended magnetohydrodynamics with embedded particle-in-cell simulation of Ganymede's magnetosphere. *Journal of Geophysical Research: Space Physics*, *121*(2), 1273–1293. https://doi.org/10.1002/2015JA021997

Zarka, P. (2007). Plasma interactions of exoplanets with their parent star and associated radio emissions. *Planetary and Space Science*, *55*(5), 598–617. https://doi.org/10.1016/j.pss.2006.05.045

Zhou, H., Tóth, G., Jia, X., & Chen, Y. (2020). Reconnection-driven dynamics at Ganymede's upstream magnetosphere: 3-D global Hall MHD and MHD-EPIC simulations. *Journal of Geophysical Research: Space Physics*, *125*(8), e28162. https://doi.org/10.1029/2020JA028162

Zhou, H., Tóth, G., Jia, X., Chen, Y., & Markidis, S. (2019). Embedded kinetic simulation of Ganymede's magnetosphere: Improvements and inferences. *Journal of Geophysical Research: Space Physics*, *124*(7), 5441–5460. https://doi.org/10.1029/2019JA026643